ARL-TR-8524 ● Sep 2018

US Army Research Laboratory

Assessment of Cavitation Models for Computational Fluid Dynamics Analysis of Erosion Risk in a Hydrocarbon-Fueled Nozzle

by Joshua Piehl and Luis Bravo

NOTICES

Disclaimers

ARL-TR-8524 ● Sep 2018

US Army Research Laboratory

Assessment of Cavitation Models for Computational Fluid Dynamics Analysis of Erosion Risk in a Hydrocarbon-Fueled Nozzle

by Joshua Piehl
Oak Ridge Associated Universities

Luis Bravo
Vehicle Technology Directorate, ARL

REPORT DOCUMENTATION PAGE	*Form Approved* *OMB No. 0704-0188*

1. REPORT DATE *(DD-MM-YYYY)* September 2018	**2. REPORT TYPE** Technical Report	**3. DATES COVERED (From - To)** 1 January 2017–31 August 2018

4. TITLE AND SUBTITLE Assessment of Cavitation Models for Computational Fluid Dynamics Analysis of Erosion Risk in a Hydrocarbon-Fueled Nozzle	**5a. CONTRACT NUMBER** **5b. GRANT NUMBER** **5c. PROGRAM ELEMENT NUMBER**
6. AUTHOR(S) Joshua Piehl and Luis Bravo	**5d. PROJECT NUMBER** **5e. TASK NUMBER** **5f. WORK UNIT NUMBER**
7. PERFORMING ORGANIZATION NAME(S) AND ADDRESS(ES) US Army Research Laboratory ATTN: RDRL-VTP Aberdeen Proving Ground, MD 21005	**8. PERFORMING ORGANIZATION REPORT NUMBER** ARL-TR-8524
9. SPONSORING/MONITORING AGENCY NAME(S) AND ADDRESS(ES)	**10. SPONSOR/MONITOR'S ACRONYM(S)** **11. SPONSOR/MONITOR'S REPORT NUMBER(S)**

12. DISTRIBUTION/AVAILABILITY STATEMENT

Approved for public release; distribution is unlimited.

13. SUPPLEMENTARY NOTES

14. ABSTRACT

Shear-driven cavitation plays an important role in many technological applications, particularly in fuel injectors for piston and gas-turbine engines. Cavitation affects the performance and longevity of fuel injectors; hence it is desirable to understand and predict its behavior since it can have favorable as well as adverse effects. Although there have been a vast number of studies, a full understanding describing its behavior has not yet been achieved. This is in part due to the complexities associated with cavitating flows, including internal flow physics, two-phase flow, and non-equilibrium thermodynamics. In this work, an assessment of the AVL-Fire computational fluid dynamics (CFD) solver coupled to an Eulerian–Eulerian cavitation model is conducted to investigate cavitation onset and the risk of erosion damage in a nozzle. The cavitation models in AVL-Fire are interrogated by comparing its ability to capture cavitation onset to experiments from a laboratory-scale optical nozzle. The models are also compared to existing CFD models across nozzle conditions in the range $20 < dP < 85$ bar using n-dodecane fuel. The models captured the cavitation process near the injector wall regions and were able to predict the critical cavitation points and the chocked flow regions, as well as quantify erosion damage. The findings will be useful to guide the design of innovative Army propulsion technologies with improved engine endurance and enhanced performance.

15. SUBJECT TERMS

cavitation, erosion, fuel, turbulence, computational fluid dynamics

16. SECURITY CLASSIFICATION OF:			**17. LIMITATION OF ABSTRACT**	**18. NUMBER OF PAGES**	**19a. NAME OF RESPONSIBLE PERSON**
a. REPORT	**b. ABSTRACT**	**c. THIS PAGE**	UU	36	Luis Bravo
Unclassified	Unclassified	Unclassified			**19b. TELEPHONE NUMBER (Include area code)** (410) 278-9719

Standard Form 298 (Rev. 8/98)
Prescribed by ANSI Std. Z39.18

Contents

List of Figures

List of Tables

Acknowledgments

This research was sponsored by a 2017 Foreign Technology (and Science) Assessment Support program award to the US Army Research Laboratory (ARL), titled “Cavitation Models for Mitigating Material Erosion in Engine Injectors”. The computational time was supported by resources from the US Department of Defense High Performance Computing Modernization Program FRONTIER Award at ARL through project “Petascale High Fidelity Simulation of Atomization and Spray/Wall Interactions at Diesel Engine Conditions”. Insightful discussions with technology-transition partners from the US Army Aviation and Missile Research, Development, and Engineering Center (AMRDEC) and Naval Air Systems Command (NAVAIR) are gratefully acknowledged.

1. Introduction

In propulsion systems, such as internal-combustion engines, the quality of liquid spray breakup is an important design factor. Improvements in fuel–air mixing lead to better combustion processes, which results in improved engine performance with reduced emissions.[1] An understanding of spray breakup requires the knowledge of the injector internal flow instabilities, which will thereby impact the spray characteristics. It has been well reported in a number of key studies[2–4] that cavitation in a shear-driven flow is a dominant factor on the atomization process in liquid fuel sprays. Hence, the ability to accurately predict the behavior of high-pressure cavitating nozzle flows is critical for propulsion and power systems, such as fuel injectors for piston engines, gas-turbines, and compact power plants.

Cavitation refers to the nucleation and growth of bubbles (or cavities) in viscous flow when the local pressure drops below the saturated vapor pressure. This commonly occurs near or on solid boundaries, due to the pressure drop caused by the rapid change in flow direction. Experiments have shown that the occurrence of cavitation in liquid injectors can lead to a better atomization efficiency[5,6] and can also limit nozzle fouling. This can be attributed to the bubble collapse or local "implosion" increasing the turbulence intensities, which in turn contribute to a faster breakup process. In contrast, cavitation is also thought to be capable of altering the injector nozzle surface through local hydro-erosion and hydro grinding.[7] This is particularly relevant for diesel engines, in light of the industry direction and performance benefits in continuously increasing fuel-injector pressures.[8] In these cases, material surface damage in the form of plastic deformation is caused by pitting, which leads to material removal through cavitation erosion. This behavior originates from the microjet impingement of the fluid induced by the local pressure changes. It has been reported that pulsating jets can reach local velocities O(100 m/s) and cause a shock on the order O(1 GPa) with a duration of 1 ns and affected area of few μm^2.[9] This violent character of the vapor cavities in a viscous flow has been extensively reviewed by Benjami and Ellis,[10] and this property has been generally accepted as the explanation of damage in solid boundaries by cavitating liquids.

Many detailed experimental and numerical studies have been conducted to investigate shear flow cavitation and advection dynamics relevant to injector flows.[11–18] The comprehensive study of Winklhofer et al.[11] has reported detailed flow and scalar field measurements of cavitation in an optical throttle under various regimes. The results show that the nozzle geometry plays a critical role affecting the size and location of bubble recirculation regimes and the velocity-pressure conditions. This study is often cited as a simulation benchmark due to its wide range of measured conditions. In a different experiment, Morozov et al.[12] conducted optical flow investigations of throttles to measure the local density and velocity field distributions near its critical cavitation point. It was reported that cavitation generates significant pressure fluctuations, with frequencies of 500 kHz, as well as pulsating flow in and downstream of the throttle. Companion simulations were also reported, using a homogeneous two-phase flow model while varying the turbulence closures to include Reynolds Averaged Navier Stokes (RANS) and the Large Eddy Simulation (LES). Here, only the LES approach was able to resolve the laminar separation with phase transition at the inlet of the throttle and the vortices in the shear layer of the jet. Dabri et al.[13] presented a total-stress criterion model for cavitating flows using an axisymmetric geometry of orifices and the level-set (LS) interface capturing model. The results showed that viscous stress has a significant effect on cavitation. It also reported larger cavitation regions and a lower cavitation number (K) with total-stress model in comparison to pressure criterion model.

Further investigations have also been conducted for more complex injector geometries. Som et al.[14] simulated the internal flow of a diesel injector using a mixture model-based approach for cavitation flow. The total stress criteria model for cavitation was utilized and evaluated under real operating conditions. The results showed overall agreement with the benchmark flow, in terms of predicting the critical cavitation points, while indicating the need for experimental data at diesel conditions. Zhao et al.[15] reported internal flow simulations using the volume of fluid (VOF) approach and flash-boiling method for cavitation. The results were validated with available throttle measurements by comparing the mass flow rates and transition points at various conditions. Although the critical cavitation point was under-predicted, the model was successfully extended to include moving needle effects on the inception dynamics. Devassy et al.[16] simulated fuel injection produced from a piezoelectric common-rail, mini-sac diesel injector nozzle. The investigation reported on the effects of compressibility, viscous heating, cavitation, and erosion modeling on the needle movement from a six-hole injector. The model used a three-phase system of liquid fuel, vapor, and air while utilizing 1-D and 3-D coupling techniques to model the injector internal flow. Liquid compressibility was revealed to be an important constituent property influencing the bubble collapse over the injector surfaces and leading to erosion. Bicer and Sou[17] explored the applicability of a Modified Rayleigh (MR) equation, based on a pressure criteria model, to predict the cavitation region and advection inside a nozzle. Comparison with conventional models and experimental data found that the MR model correctly predicts cavitation with respect to cavity length and thickness when using a combined VOF–MR coupled to a RANS approach for low Reynolds number flows.

In summary, these investigations provide important research directions to develop improved cavitation and erosion models.

Although significant progress has been made with experimental visualization techniques, it remains very difficult to observe the flow state with sufficient resolution. Furthermore, optical flow data produced from real diesel injectors remain scarce. Hence, there is a critical need to complement measurements with numerical investigations that are able to describe the cavitation dynamics to probe and better understand its behavior. The objective of this report is to assess the ability of the AVL-Fire computational fluid dynamics (CFD) solver to predict the onset of cavitation and erosion damage. To accomplish this, three cavitation models, Original FIRE, Schnerr and Sauer,[18] and Singhal et al.[19] were interrogated to document its ability to predict cavitation and erosion in internal flows. The simulation results are compared with the Winklhofer experimental data from the literature.[11] The results, in terms of a validated framework, will be used to guide improved design models.

2. Problem Identification and Challenges

Engine failures due to erosion in cavitating injectors are drastically impacting the effectiveness of the Army mission. Fuel injectors are a critical component used widely in both aerial and terrestrial vehicles operating with reciprocating (piston) or gas-turbine engines fueled with JP-8 or F-24. The Gray Eagle MQ-1C Unmanned Aircraft System and the Joint Light Tactical Vehicle are two examples where this type of damage risk is relevant. Cavitation damage significantly alters the material state (and shape) and leads to erosion, which may cause injector failure and a significant loss of vehicle power. Alterations to nozzle geometry shapes, which have been designed for optimized conditions, will degrade the flow behavior and discharge efficiency. Figures 1 and 2 show the cavitation damage on diesel injector geometries in areas including the discharging orifice, needle valve, and the sac volume. Figure 1a shows the schematic of a valve-covered orifice (VCO) nozzle tip. Figure 1b–c shows the damaged regions at the top part of the injector hole and at the two sides of the orifice.

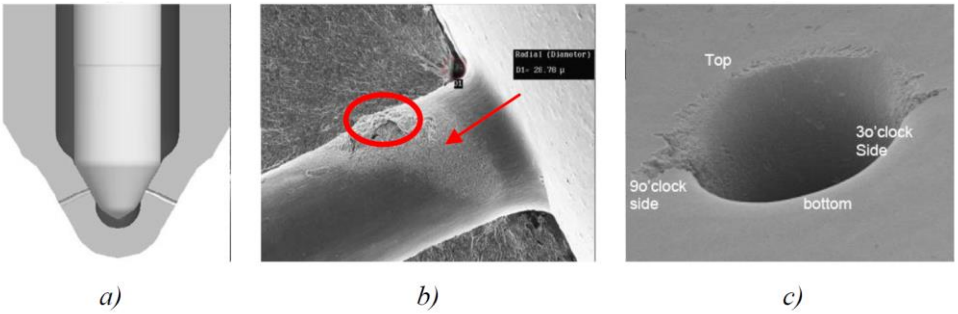

a) b) c)

Fig. 1 Cavitation-induced erosion damage a) schematic of a VCO nozzle, b) picture of erosion damage at the top part of injection hole, and c) erosion damage at the two sides of injection hole

Figure 2 shows cavitation damage in an SAC-type diesel nozzle along with the damage on the needle. This suggests that cavitation damage is present in both types of engine injectors relevant to diesel engines. Existing CFD tools have been historically limited in their ability to accurately predict cavitation inception, material surface erosion, and potential injector damage. It also remains extremely challenging to measure internal nozzle flows due to the restrictive geometry and camera inaccessibility. Experiments on cavitating flows and subsequent erosion or its influence on spray discharge are limited. Hence, there is a need to quantify and understand its behavior to create concept designs that mitigate its occurrence.

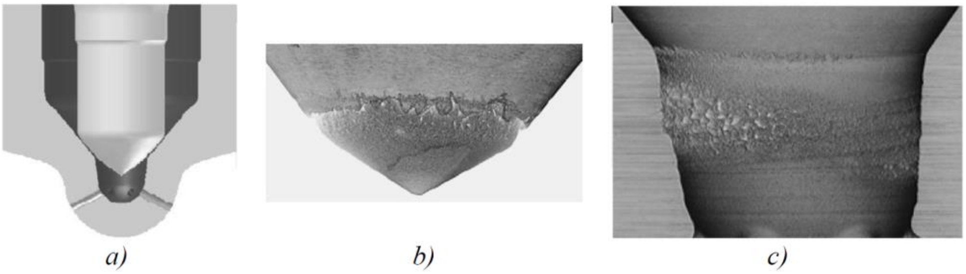

a) b) c)

Fig. 2 Cavitation-induced erosion damage: a) schematic of sac-type nozzle, b) picture of erosion damage on needle, and c) erosion damage on the sac volume

There are still various barriers including the ability to accurately design meshing structures that capture the flow scales, and inception points. It is not known a priori what the bubble length-scales are; hence, creating an accurate grid can be a challenge, especially for various designs and concept development. In addition, the models have not been fully explored in all possible scenarios; hence, it is expected that significant input will be required to parameterize the model and validate the outcomes. Assessment of this technology will establish the ability to predict the complex flows through extensive parameterization of problems of interest that will provide guidelines for accurate modeling, and physical prototype concept development.

3. Governing Equations

In this study, the AVL-Fire Eulerian–Eulerian multifluid model is adopted to simulate the unsteady two-phase flow dynamics. This model is utilized for an n-phase system to simulate cavitation in a fuel nozzle.[20,21] In the multifluid model, the time-accurate conservation equations for compressible flow are solved for each phase separately. The model is based on the formulation presented in Drew and Passman[22] and Lahey and Drew.[23] In addition, Kunz et al.[24] and Carrica et al.[25] provided a robust and time-accurate numerical method for multiphase flow on unstructured grids. The continuity and momentum equations are presented as follows:

$$\frac{\partial \alpha_k \rho_k}{\partial t} + \nabla \cdot \alpha_k \rho_k \boldsymbol{v}_k = \sum_{l=1, l\neq k}^{N} \Gamma_{kl} \;\; k = 1, \dots, N \tag{1}$$

$$\begin{gathered}\frac{\partial \alpha_k \rho_k \boldsymbol{v}_k}{\partial t} + \nabla \cdot \alpha_k \rho_k \boldsymbol{v}_k \boldsymbol{v}_k = -\alpha_k \nabla p_k + \nabla \cdot (\boldsymbol{\tau}_k + \boldsymbol{T}_k^t) \\ + \alpha_k \rho_k \boldsymbol{g} + \sum_{l=1, l\neq k}^{N} \boldsymbol{M}_{kl} + \sum_{l=1, l\neq k}^{N} \boldsymbol{v}_{ki} \Gamma_{kl}\end{gathered} \tag{2}$$

$\boldsymbol{v}_{ki}$ is velocity at the interface, Γ_{kl} is mass interfacial exchange between phases *k* and *l* and α_k is the volume fraction of phase *k*, which equals

$$\sum_{k=1}^{N} \alpha_k = 1. \tag{3}$$

Since the pressure is assumed to be the same for all the phases,

$$p_k = p, \tag{4}$$

$\boldsymbol{M}_{kl}$,$\boldsymbol{\tau}_k$, and $\boldsymbol{T}_k^t$, are the interfacial momentum exchange, shear stress, and the Reynolds stresses, between phases *k* and *l*:

$$\boldsymbol{M}_{kl} = C_{TD} \rho_k k_k \nabla \alpha_l + \frac{1}{8} C_D \rho_k A_i''' |\boldsymbol{v}_r| \boldsymbol{v}_r = -\boldsymbol{M}_{lk} \tag{5}$$

$$\boldsymbol{\tau}_k = \mu_k [(\nabla \boldsymbol{v}_k + (\nabla \boldsymbol{v}_k)^T) - \frac{2}{3} \nabla . \boldsymbol{v}_k \boldsymbol{I}] \tag{6}$$

$$\begin{gathered}\boldsymbol{T}_k^t = -\rho_k \overline{v'_k v'_k} = \mu_k^t [(\nabla \boldsymbol{v}_k + (\nabla \boldsymbol{v}_k)^T) - \\ \frac{2}{3} \nabla \cdot \boldsymbol{v}_k \boldsymbol{I}] - \frac{2}{3} \rho_k k_k \boldsymbol{I}.\end{gathered} \tag{7}$$

C_{TD}, C_D, A_i''', $\boldsymbol{v}_r$, and μ_k^t are turbulent dispersion, drag coefficient, interfacial area density, relative velocity between phases ($\boldsymbol{v}_r = \boldsymbol{v}_k - \boldsymbol{v}_l$), and turbulent viscosity respectively. Turbulent viscosity, μ_k^t, is modeled as

$$\mu_k^t = \rho_k C_\mu \frac{k_k^2}{\varepsilon_{k.}} \tag{8}$$

Conservation equation of total enthalpy is

$$\begin{gathered}\frac{\partial \alpha_k \rho_k h_k}{\partial t} + \nabla \cdot \alpha_k \rho_k \boldsymbol{v}_k h_k = \nabla \cdot \alpha_k (q_k + q_k^t) + \alpha_k \rho_k q_k''' \\ + \alpha_k \rho_k \boldsymbol{g} \cdot \boldsymbol{v}_k + \nabla \cdot \alpha_k (\boldsymbol{\tau}_k + \boldsymbol{\tau}_k^t) \cdot \boldsymbol{v}_k + \alpha_k \frac{\partial p}{\partial t} \\ + \sum_{l=1, l\neq k}^{N} H_{kl} + \sum_{l=1, l\neq k}^{N} h_{ki} \Gamma_{kl,}\end{gathered} \tag{9}$$

where $q_k, q_k''', h_{ki}, H_{kl}$ are heat flux, volumetric enthalpy source, enthalpy of phase k at the interface, and interfacial energy exchanges between phases k and l, respectively. The superscript *t* represents the turbulent contributions. The turbulent kinetic energy is as follows:

$$\begin{gathered}\frac{\partial \alpha_k \rho_k k_k}{\partial t} + \nabla \cdot \alpha_k \rho_k \boldsymbol{v}_k k_k = \nabla \cdot \alpha_k \left(\mu_k + \frac{\mu_k^t}{\sigma_k} \right) \nabla k_k \\ + \alpha_k T_k - \alpha_k \rho_k \varepsilon_k + \sum_{l=1, l\neq k}^{N} K_{kl} + \sum_{l=1, l\neq k}^{N} k_{ki} \Gamma_{kl}\end{gathered} \tag{10}$$

where K_{kl} and k_{ki} are the turbulent interfacial exchange and kinetic energy of phase k at interface accordingly. T_k is the production term due to the shear stress. It is defined as

$$T_{\boldsymbol{k}} = \boldsymbol{T}_{\boldsymbol{k}}^{\boldsymbol{t}} : \nabla \boldsymbol{v}_{\boldsymbol{k}}. \tag{11}$$

The turbulent dissipation rate equation is equal to

$$\begin{gathered}\frac{\partial \alpha_k \rho_k \varepsilon_k}{\partial t} + \nabla \cdot \alpha_k \rho_k \boldsymbol{v}_k \varepsilon_k = \nabla \cdot \alpha_k \left(\mu_k + \frac{\mu_k^t}{\sigma_\varepsilon} \right) \nabla \varepsilon_k \\ + \sum_{l=1, l\neq k}^{N} D_{kl} + \sum_{l=1, l\neq k}^{N} \varepsilon_{ki} \Gamma_{kl} + \alpha_k C_1 P_k \frac{\varepsilon_k}{k_k} \\ - \alpha_k C_2 \rho_k \frac{\varepsilon_k^2}{k_k} + \alpha_k C_4 \rho_k \varepsilon_k \nabla \cdot \boldsymbol{v}_k.\end{gathered} \tag{12}$$

D_{kl} is the dissipation rate interfacial exchange between phases *k* and *l*.

3.1 Cavitation Models

Three cavitation models, Original FIRE, Schnerr and Sauer,[18] and Singhal et al.,[19] were used to solve the interfacial mass exchange Γ_{kl}.

3.1.1 Original FIRE Model

$$\Gamma_c = -\Gamma_d = \begin{cases} C_e \rho_d (3\alpha_d)^{2/3} (4\pi N''')^{1/3} |\dot{R}| & \Delta P \geq 0 \\ -\dfrac{1}{C_r} \rho_d (3\alpha_d)^{2/3} (4\pi N''')^{1/3} |\dot{R}| & \Delta P < 0 \end{cases} \tag{13}$$

Subscripts c and d denote the continuous and dispersed phase correspondingly. N''' is the bubble number density, $\dot{R}$ is bubble growth and collapse rate, C_e is the cavitation enhancement factor, and C_r is the condensation reduction factor.

These empirical coefficients can be used to either increase the evaporation or decrease the condensation rate. It accounts for model uncertainties due to the lack of detailed experimental data available and limiting model assumptions. It is important to note that bubble number density is defined as

$$N''' = \frac{N'}{V}, \tag{14}$$

where N' is the number of bubbles and V is the volume of the cell. The closure of the problem is obtained with a further relation for the bubble number density:

$$N''' = \begin{cases} N_0''' & \alpha_l \leq 0.5 \\ 2(N_0''' - 1)(1 - \alpha_l) + 1 & \alpha_l > 0.5, \end{cases} \tag{15}$$

where N_0''' is the initial bubble number density and depends on the characteristics of liquid-phase. The bubble number density for water varies from 10^9 to 10^{15} sites per unit volume,[26] and it was set to 10^{12} as suggested by Fujimoto et al.[27]

3.1.2 Schnerr and Sauer et al. Model

$$\Gamma_c = -\Gamma_d = \begin{cases} C_e \dfrac{\rho_d \rho_c}{\alpha_d \rho_d + \alpha_c \rho_c} \alpha_c (3\alpha_d)^{2/3} (4\pi N''')^{1/3} |\dot{R}| & \Delta P \geq 0 \\ -\dfrac{1}{C_r} \dfrac{\rho_d \rho_c}{\alpha_d \rho_d + \alpha_c \rho_c} \alpha_c (3\alpha_d)^{2/3} (4\pi N''')^{1/3} |\dot{R}| & \Delta P < 0 \end{cases} \tag{16}$$

Closure relation for the bubble number density is

$$N''' = (1 - \alpha_d) N_0'''. \tag{17}$$

3.1.3 Singhal et al. Model

$$\mathit{\Gamma}_c = -\mathit{\Gamma}_d = \begin{cases} C_e \dfrac{\rho_d \rho_c}{\alpha_d \rho_d + \alpha_c \rho_c} \alpha_c \rho_c \dfrac{\sqrt{k}}{\phi} |\dot{R}| & \Delta P \geq 0 \\ -\dfrac{1}{C_r} \dfrac{\rho_l \rho_k}{\alpha_d \rho_d + \alpha_c \rho_c} \alpha_d \rho_c \dfrac{\sqrt{k}}{\phi} |\dot{R}| & \Delta P < 0, \end{cases} \tag{18}$$

where ϕ is the bubble surface tension and k is the local turbulent kinetic energy.

To obtain interfacial mass exchange between two phases for any of the previously mentioned cavitation models, bubble growth and collapse rate should be solved, which is governed by Rayleigh–Plesset equation,[28]

$$|\dot{R}| = \sqrt{\frac{2}{3} \frac{|\Delta p|}{\rho_c} - R\ddot{R}}, \tag{19}$$

where Δp is the effective pressure difference, which is equal to

$$\Delta p = p_{sat} - \left(p - C_E \frac{2}{3} \rho_c k_c\right). \tag{20}$$

C_E is the Egler coefficient, which depends on the local turbulence level.[29] The value can be taken between 0.3 to 1.4 depending on the application.[30]

Egler factor (C_E), cavitation enhancement factor (C_e), and condensation reduction factor (C_r) were modified to better predict the measured data as shown in Table 1.

Table 1 Coefficients of various cavitation models

Coefficient	Original FIRE	Singhal	Schnerr and Sauer
$\boldsymbol{C_E}$	0.8	0.3	0.3
$\boldsymbol{C_e}$	1	0.02	1
$\boldsymbol{C_r}$	100	100	100

3.2 Cavitation Erosion Models

The erosion model is based on the work of Berchiche et al.[31] and Franc and Riondet.[32] The mean depth of penetration rate (MDPR) and the incubation time (T_i) are the two key output variables.[30] Incubation time measures the exposure time before the onset of mass loss, and MDPR measures the rate of material removal from the surface at a steady state, after the incubation time. MDPR is as follows:

$$MDPR = N.S.\Delta L = N.S.L\left[\left(\frac{\varepsilon'}{\varepsilon_U}\right)^{1/\theta} - 1\right], \tag{21}$$

where $N, S, L,$ and θ represent the impacts per unit area, size of the impact loads, the maximum thickness of the hardened layer, and the shape factor, respectively. $\varepsilon'$and ε_U are surface strain rate and ultimate strain rate, which are linked to their corresponding stresses as

$$\sigma = \sigma_Y + K \cdot \varepsilon^n \longrightarrow \varepsilon = \left[\frac{\sigma - \sigma_Y}{K}\right]^{1/n}. \tag{22}$$

σ_Y is the yield stress, K is the K-factor and n is the stress-strain relation exponential factor, which they depend on the material properties. The surface strain rate ε' is obtained from energy consideration. The energy absorbed by the material is

$$W(\varepsilon) = lS\varepsilon\left[\frac{\sigma_Y}{1+\theta} + \frac{K\varepsilon^n}{(1+n)(1+\theta+n\theta)}\right], \tag{23}$$

where l is the the thickness of hardened layer. At steady state after the incubation period,

$$W(\varepsilon') = W(\varepsilon_1) + W(\varepsilon_U), \tag{24}$$

where ε_1 is computed from Eq. 22 with the stress estimated by

$$\sigma_1 = MIN(C_p s \rho_l \frac{dr_b}{dt}, \sigma_{max}), \tag{25}$$

where C_p is the proportionality constant, s is the liquid's speed of sound, and σ_{max} is the above maximum stress allowed for the material.

Incubation time, T_i, is given by

$$T_i = \frac{1}{N\,S}\left[\frac{\sigma_U - \sigma_Y}{\sigma - \sigma_Y}\right]^{\frac{1+\theta}{n\theta}} \times \frac{(1+n)(1+\theta+n\theta)\sigma_Y + (1+\theta)(\sigma_U - \sigma_Y)}{(1+n)(1+\theta+n\theta)\sigma_Y + (1+\theta)(\sigma - \sigma_Y).} \tag{26}$$

In the current report, the Eulerian-Eulerian multi-fluid model is coupled with cavitation and erosion models to simulate the vulnerability (damage) areas in a fuel nozzle. Transitionary and turbulent flow is modeled using the classical Reynolds Averaged Navier Stokes Equation model (RANS-$k - \varepsilon$), not included here for brevity. The cavitation characteristics, in terms of mass-flow-rates and critical cavitation regimes, are compared with benchmark data from the literature.[11]

4. Experimental Benchmark

In this work, the nozzle of Winklhofer et al.[11] has been used for the experimental measurement. In the experiments, the nozzle design was created on a 0.3-mm sheet of steel between two sapphire windows. The nozzle was 1 mm long with an inlet width of 0.301 mm and an exit width of 0.284 mm. The inlet had chamfered edges with a radius of 20 µm. The geometry of the experimental rig is seen in Fig. 3. Here the pressure drop across the nozzle was varied to identify the transition into chocked flow regions. The pressure drops of ΔP = 20, 40, 60, 70, 75, 80, and 85 bar were utilized. The pressure at the inlet was held constant at 100 bar and the outlet pressure was adjusted for various cases starting from 80 bar to 15 bar. The transition from pressure-dependent mass flow rate to chocked mass flow defines the critical cavitation (CC) point.[11]

Dodecane fuel was used for this study. The physical properties of the fuel are held constant to reduce the computational expense associated with running the simulation. Holding the physical properties of the fuel constant will increase the occurrence of cavitation in the simulation to that of a "worst-case" scenario for an experimental run.[10] Furthermore, the physical properties of the gas vary depending on the ambient conditions as these conditions will affect the gas density. The properties of the fuel are summarized in Table 2.

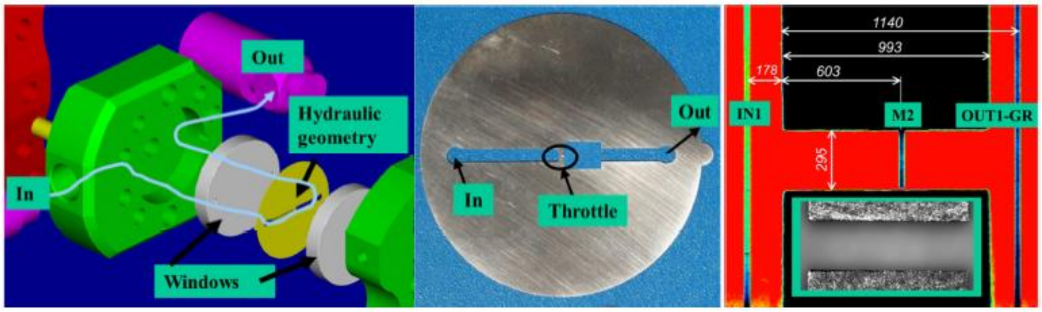

Fig. 3 Images of experimental nozzle and setup[11]

Table 2 Physical properties of the liquid and gas phase in the simulation. Note that the gas phase properties varied with temperature and pressure.

Property	Liquid phase	Gas phase
Fluid	Dodecane	Dodecane Vapor
Density (kg/m^3)	830	7
Viscosity (Pa.s)	2.14e-3	1e-5
Specific heat (J/kg-K)	2210	1000
Thermal conductivity (W/mK)	0.134	0.03

5. Computational Results

5.1 Determination of Finite Volume Cell-Size Distribution

Mesh size sensitivity was analyzed by modeling the fuel nozzle flow at a single operating condition of ($\Delta P = 80\,\text{bar}$) with the same geometry but different unstructured mesh cell sizes. The grid distributions are shown in Fig. 4 and they vary from fine grid (Case 1) to coarse grid (Case 4). The range of min cell sizes reported are 6.13, 7.55, 9.48, and 13.40 µm, which resolve the shear layers to different degrees. Winklhofer[11] reported critical mass flow rate of 7.82 g/s, which is now used to assess the model accuracy.

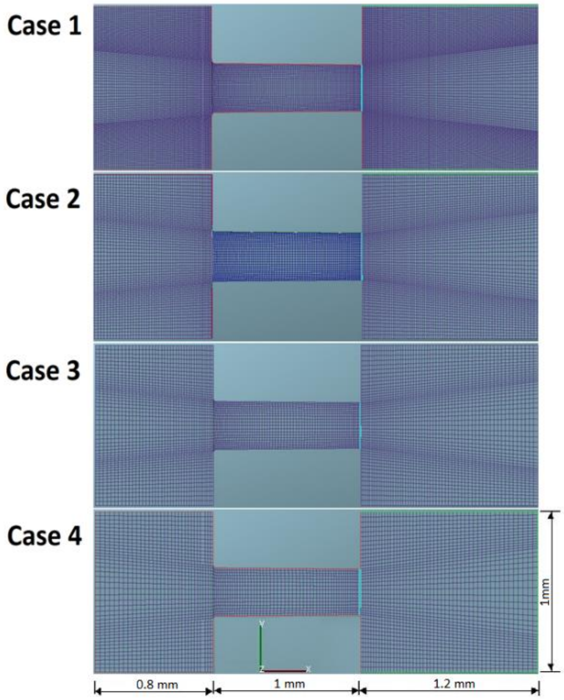

Fig. 4 Grid distributions for mesh sensitivity analysis: Case 1) min dx = 6.13 µm, 2) min dx = 7.55 µm, 3) min dx = 9.48 µm, and 4) min dx = 13.40 µm

Table 3 shows the min/max cell size, total cell count, wall-clock time, and the difference in critical mass flow rate with respect to measured data. As shown in the table, the mass flow rate is not dependent on mesh cell size, and it is in good agreement with the measured data within a 3% error margin. However, as shown in Fig. 5, more flow structure, in terms of the total kinetic energy in the shear layers, can be captured by using finer mesh sizes.

Table 3 Effect of cell size on the nozzle mass flow rate

Case	1	2	3	4
Number of meshes	690,000	215,080	96,000	49,260
Min. mesh size (μm)	6.13	7.55	9.48	13.40
Max. mesh size (μm)	15.07	22.51	27.99	34.39
Mass flow rate difference (%)	2.35	2.38	3.00	3.02
Wall time (h)	81.35	15.82	9.56	2.22

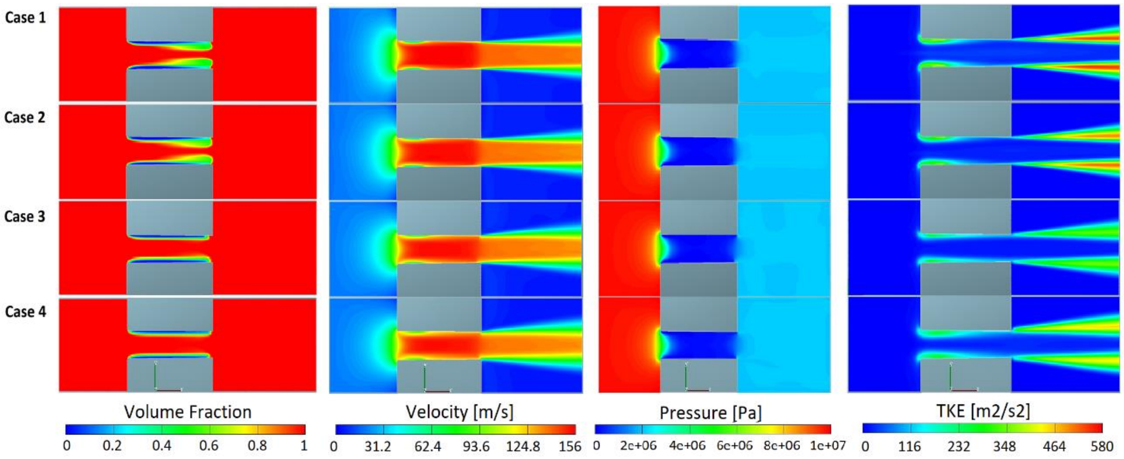

Fig. 5 Simulation results of volume fraction of liquid phase, velocity, pressure, and turbulent kinetic energy for various mesh cell sizes at $\Delta P = 80$ bar. RANS and Singhal et al.[19] cavitation model were used for simulation.

Since the results of the Cases 1 and 2 (Table 3) are nearly identical, and Fig. 5 does not show much difference in terms of flow structure, the Case 2 grid distribution (total cell count 215,080) is recommended to perform the model assessment.

5.2 Cavitation Model Assessment

The Singhal et al.[19] cavitation model was used to investigate the incipient of cavitation and the critical cavitation point by using various pressure drops of 60, 70, 75, 78, 79, 80, and 85 bar between the nozzle inlet and outlet. Critical cavitation point is termed as the point at which the increase in pressure drop does not have any effect on mass flow rate.[11] At this condition, cavitation develops rapidly in the nozzle at just 1 bar higher pressure drop and the nozzle gets clogged with vapor.[11] Therefore, this condition results in a constant mass flow rate (choked flow) regardless of increasing the pressure drop. The critical pressure drop for the studied case is measured to be 71 bar.[11] The simulated results overpredicted the pressure drops at cavitation condition as shown in Fig. 6. The measured mass flow rate at this condition is 7.82 g/s at 71 bar and the current simulation data is 8.01 g/s at 78 bar. At one bar higher, 79 bar, cavitation blocks the nozzle exit leading to the choked flow (plateau flow region). In the current work, the overall behavior of the mass flow rates were in very good agreement with experimental results compared to the literature.[14,15] The simulation is able to capture the occurrence of a CC point, which is noteworthy in light of the lack of experimental uncertainty provided from the measurements. The difference between the simulated and measured mass flow rate and critical cavitation point could be due to the different fuel utilized by Winklhofer et al.,[11] in which the fuel properties were not reported. The behavior of cavitation onset is shown in Fig. 7 via visualizations of the liquid volume fractions at various pressure drops. The vapor region significantly increases near the wall and in the streamwise direction with higher pressure drop.

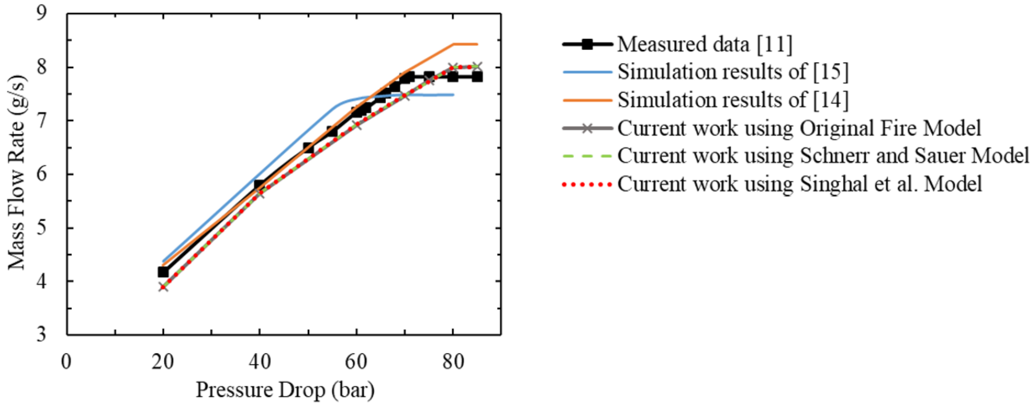

Fig. 6 **Mass-flow-rate comparison between simulated cavitation models and measured data**

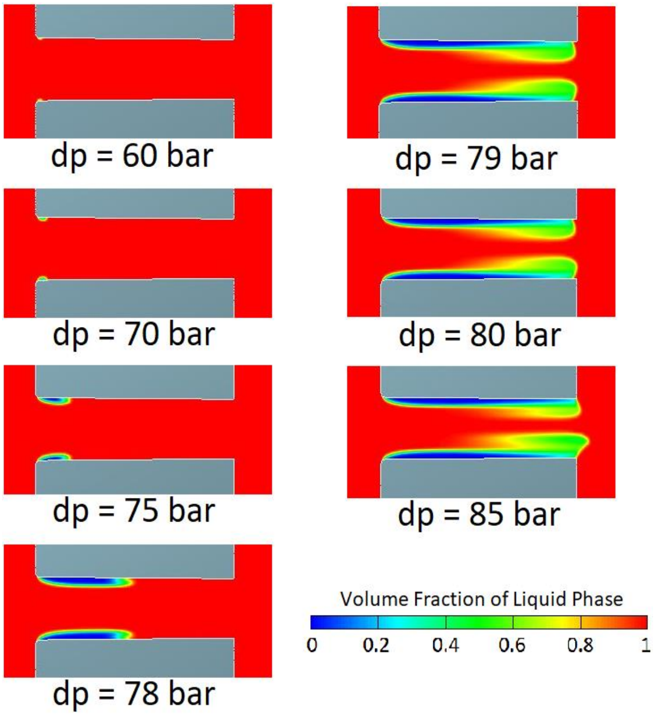

Fig. 7 Liquid volume fraction at several pressure drops using the Singhal et al.[19] cavitation model and RANS.

Original FIRE and Schnerr and Sauer[12] were also employed to model the Winklhofer et al.[11] nozzle geometry to determine the effect of cavitation models on the prediction of critical cavitation regions and mass flow rate analysis. It was observed that the three models predict similar behavior and mass flow rates for the pressure drops considered, Δp = 20, 40, 60, 70, 75, 80, and 85 bar. As shown in Fig. 6, the mass flow rates of the three AVL cavitation models were compared with the measured data as well as the simulation results presented in Som et al.[14] and Zhao et al.[15] It was found that all AVL cavitation models correctly predict the pressure dependency mass-flow-rate region, up to a critical point of 75 bar, but overpredict it in the choked flow region (between 75 and 85 bar) with respect to the measurements. In Zhao et al.,[15] the simulation result shows a critical point at 65 bar and underpredicts the choked mass flow rate afterward. The results presented in Som et al.[14] obtained a critical point at 80 bar as well as an overprediction of the choked mass flow rate.

The behavior of the liquid volume fractions at various pressure drops is shown in Fig. 8 through visualization of the volume fraction. All models captured cavitation near the solid boundary region and presented similar advection characteristics with some interesting differences. Specifically, liquid volume fraction estimated by the Singhal et al.[19] model predicted more vapor region at the nozzle exit, which is consistent with the measurements. However, at Δp = 70 bar, the models captured the vapor pockets only in regions near the nozzle inlet. These discrepancies were also reported in Som et al.[14] and Zhao et al.[15] Further work is underway to understand the experimental and model parameter uncertainties to better explain the differences. It should be noted that the current CFD technique used at the US Army Research Laboratory (ARL)[33] shows two distinct features: It predicts a thinner cavitation region near the injector wall, but higher vapor distribution in the center of the nozzle.

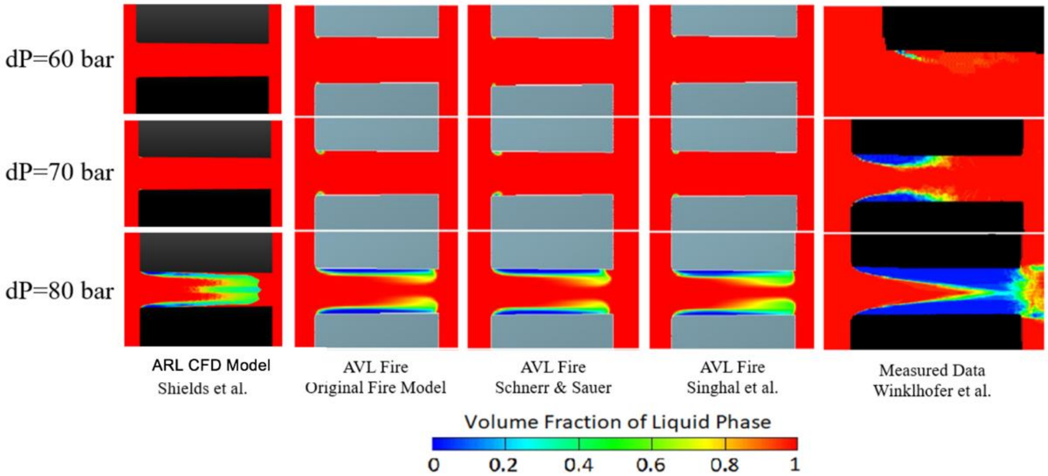

Fig. 8 Effect of cavitation models on the prediction of cavitation region at various pressure drops. The data were measured using shadowgraph technique.[11]

In Fig. 9, velocity profiles in the nozzle at 53 µm from the nozzle entrance are compared with the available measured data at the pressure drops of 55 bar, without cavitation, and 67 bar, with a small cavitating flow region. The velocity profile is almost symmetrical about the center of the nozzle, which is anticipated due to the symmetrical geometry. Due to the high circulation regime at the boundary layer interface, shear layer is maximum at approximately 40 and 46 µm from the wall toward the nozzle center where the velocity peaks for $\Delta p = 55$ and $\Delta p = 67$ bar, respectively. It is evident that the models can simulate the flow in the nozzle accurately compared with the measured data from Winklhofer et al.[11]

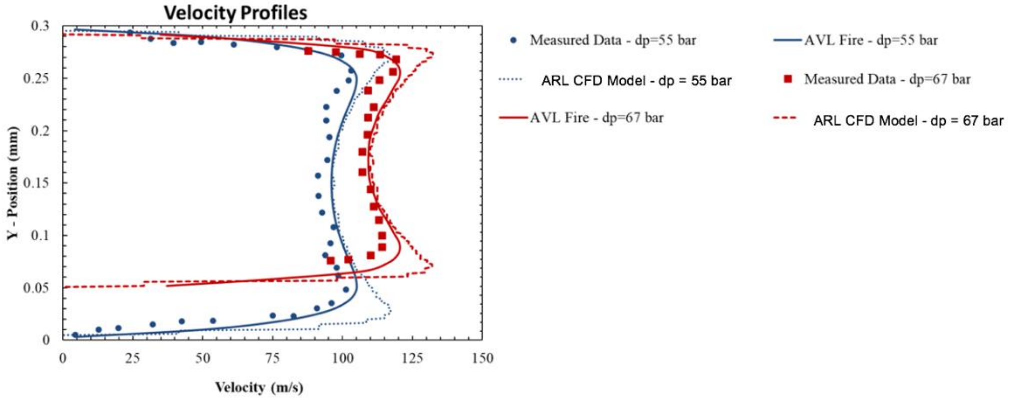

Fig. 9 Velocity profile in the nozzle at 53 µm from the nozzle inlet at the pressure drops of 55 and 67 bar in comparison with measured data from Winklhofer et al.[11] The Original FIRE model was used for cavitation simulation.

5.3 Erosion and Material Damage Assessment

To identify vulnerability or damage zones in nozzles, results from the erosion model are presented for a reference case. Three phases of the erosion process versus time are shown in Fig. 10[30] including the incubation time, acceleration period, and steady period. The incubation time is the period of cavitation exposure before any damage occurs. The MDPR is the steady-state material removal that peaks after the incubation time and the acceleration period as shown in Fig. 10. The region of bubble collapse in the nozzle is calculated by using the two governing parameters of volume fraction threshold of erosion, and critical distance of bubble collapse. The former specifies the vapor volume fraction below which the collapse occurs, and the latter determines the distance from the wall within which the collapse has a damaging effect. The volume fraction threshold of 0.05 and the critical distance of 5 µm were taken from the AVL FIRE manual[30] and used in this work. Additionally, Stainless Steel 316L property was used for the assessment of erosion modeling and material properties were taken from Berchiche et al.[31]

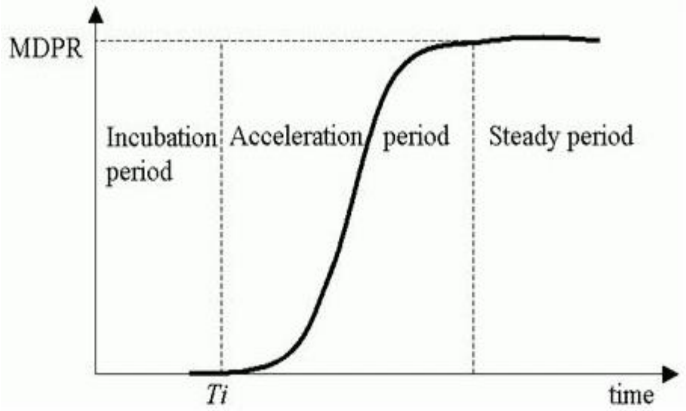

Fig. 10 Erosion process phases, adapted from AVL FIRE manual [30]

The computational analysis is conducted by coupling the AVL Original cavitation model (described in Section 3.1.1) and the erosion model (see Section 3.2). The results are extracted and time-averaged during the steady state period, obtained approximately after 5–10 non-dimensional flow through time scales. To report on model performance across a broad range of parameters, the operating conditions considered here are *dP* = 70, 75, 78, 80, and 85 bar since we reported significant amounts of cavitation cloud regions in the nozzle. Figures 11 and 12 show the spatial contours and averaged point values of the MDPR respectively at each operating point. Material surface erosion is presented in terms of averaged MDPR and it is indicative of the damage as a result of the fluid-energy exchange mechanism of cloud collapse at the solid boundary. As shown in Fig. 11, the vulnerability zones are strongly dependent on the operating conditions considered. In this nozzle geometry, damage will occur in regions extending from the center inlet to the nozzle exit location and correlate with regions of pronounced cavitation intensity. Thus, the maximum damage will occur in the closure area of the vapor region, where bubbles are more likely to collapse, and increased levels of vorticity and turbulence production are present. The red color indicates the progression of peak MDPR regions prone to the material erosion damage.

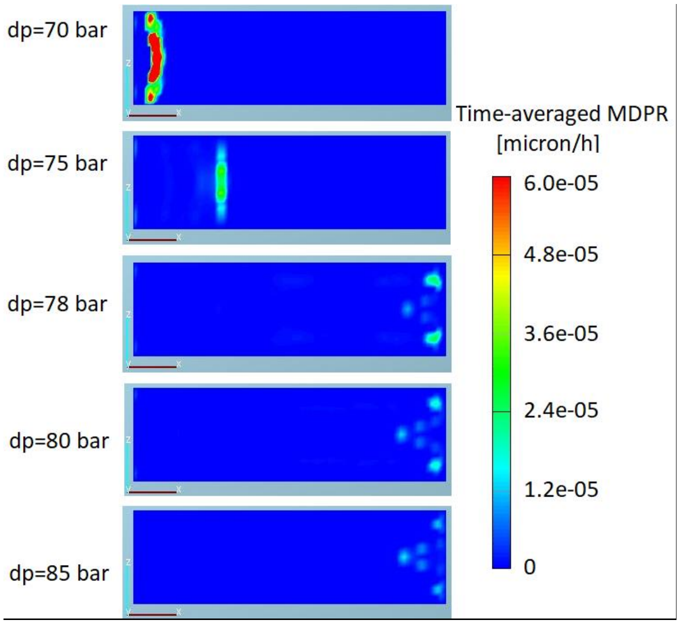

Fig. 11 Time-averaged MDPR contours at pressure drops of 70, 75, 78, 80, and 85 bar by using RANS and Original FIRE model at steady state condition. The data are time averaged with span of 1 ms.

Figure 12 shows the maximum values of the MDPR variations with the operating conditions considered. The peak penetration rate is reported at $6x10^{-4}$ micros/h occurring at *dP* = 70 bar and a significant rate reduction is observed (by a factor of 6) when the operating condition reaches *dP* = 75bar. This increase in operating pressure condition corresponds to the growth of the cavitation zone regions in terms of surface area near the solid boundary (see Fig. 7). Further increases in the pressure drop only moderately affect the damage in terms of MDPR with the least effect observed from *dP* = 80 to *dP* = 85 bar.

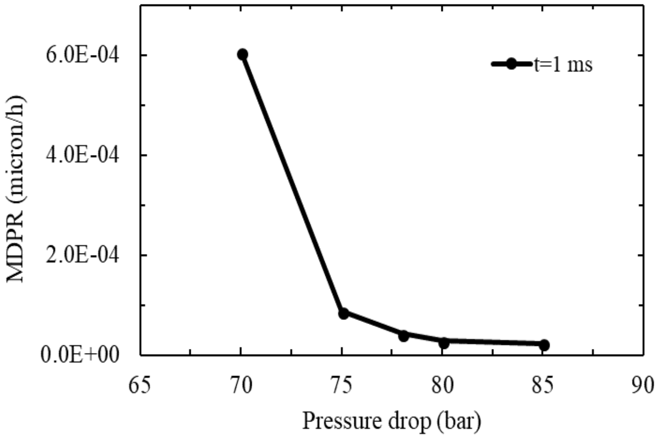

Fig. 12 Effect of pressure drop on MDPR using Original Fire model

Further, the effect of pressure operating conditions on the incubation time for parameters are presented in Fig. 13. The incubation time grows substantially with increased cavitation zone regions, consistent with the MDPR results. Slower MDPR values indicate a growth in cavitation area and a significant decrease of the local fluid-energy exchange mechanism (increased vorticity and rate of turbulence production) that occurs near the solid during the vapor cloud collapse. The incubation time growth is consistent with the cavitation dynamics and evolution of the damage zone in the nozzle that are dependent on the operating conditions.

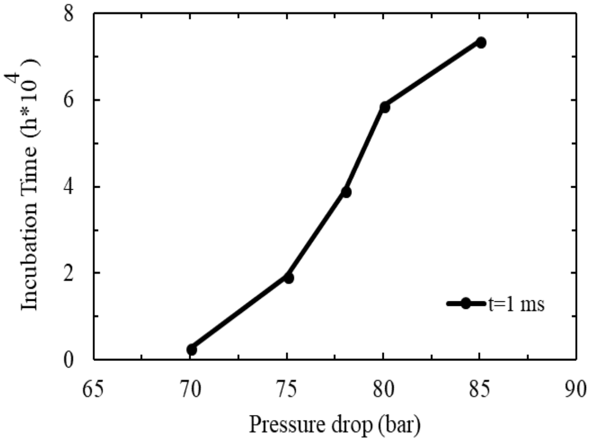

Fig. 13 Effect of pressure drop on incubation time (T_i) using Original FIRE model

5.4 Sensitivity Analysis of Erosion Governing Parameters

The effects of cavitation coefficients, Egler Factor (C_E), cavitation enhancement factor (C_e), and cavitation reduction factor (C_r), on the mass flow rate, cavitation number, and cavitation region were studied by using the Original FIRE cavitation model. The simulations were performed at two operating conditions, *dP*= 78 and *dP* =80 bar. The test matrix is shown in Table 4.

Table 4 Utilized cavitation coefficients for sensitivity analysis

	Default values	Set A	Set B	Set C
C_E	0.3	0.4, 0.8, 1.2	0.8	0.8
Ce	1	1	0.1, 1, 10	1
Cr	1	100	100	1, 10, 100

The mass flow rate and cavitation number does not change to a great extent by varying the Egler factor (C_E), as shown in Fig. 14a. Additionally, the cavitation regions are very similar at both 78 and 80 bar pressure drops, as shown in Fig. 15a.

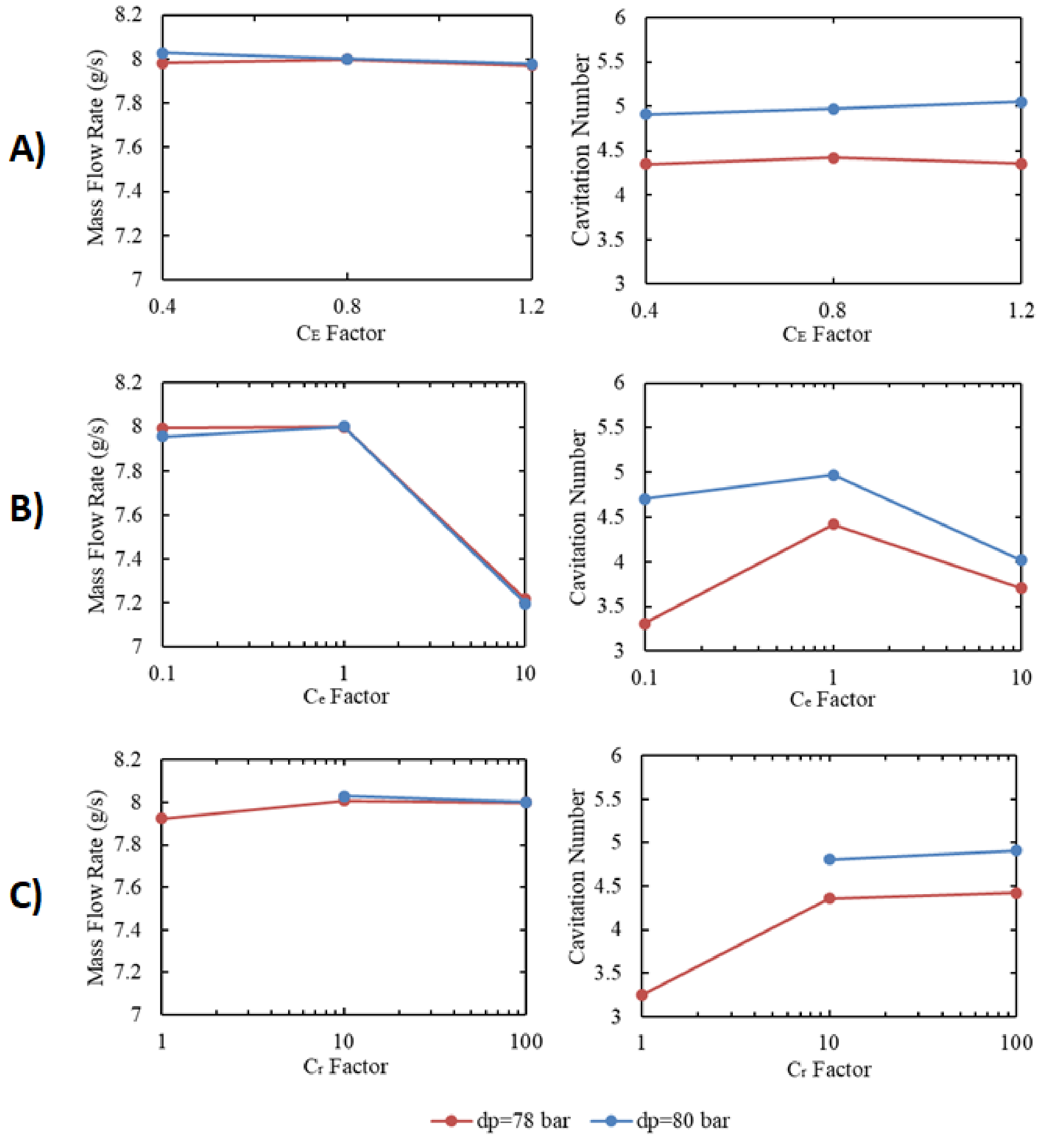

Fig 14 Effects of C_E, C_e, and C_r on the mass flow rate, and cavitation number using coefficient sets of Table 4 at the pressure drops of 78 and 80 bar

As shown in Fig. 14b, the mass flow rate and cavitation number increase by increasing the cavitation enhancement factor (C_e) until C_e reaches one, followed by a sharp decrease. This decrease does not follow the physics behind cavitation since we expect the cavitation number to increase with larger cavitation enhancement factor (C_e). The cavitation region at various C_e are shown in Fig. 15b and the region increases by increasing the enhancement factor up to one. Hence, it is suggested to use a value between 0.1 and 1 for the enhancement factor.

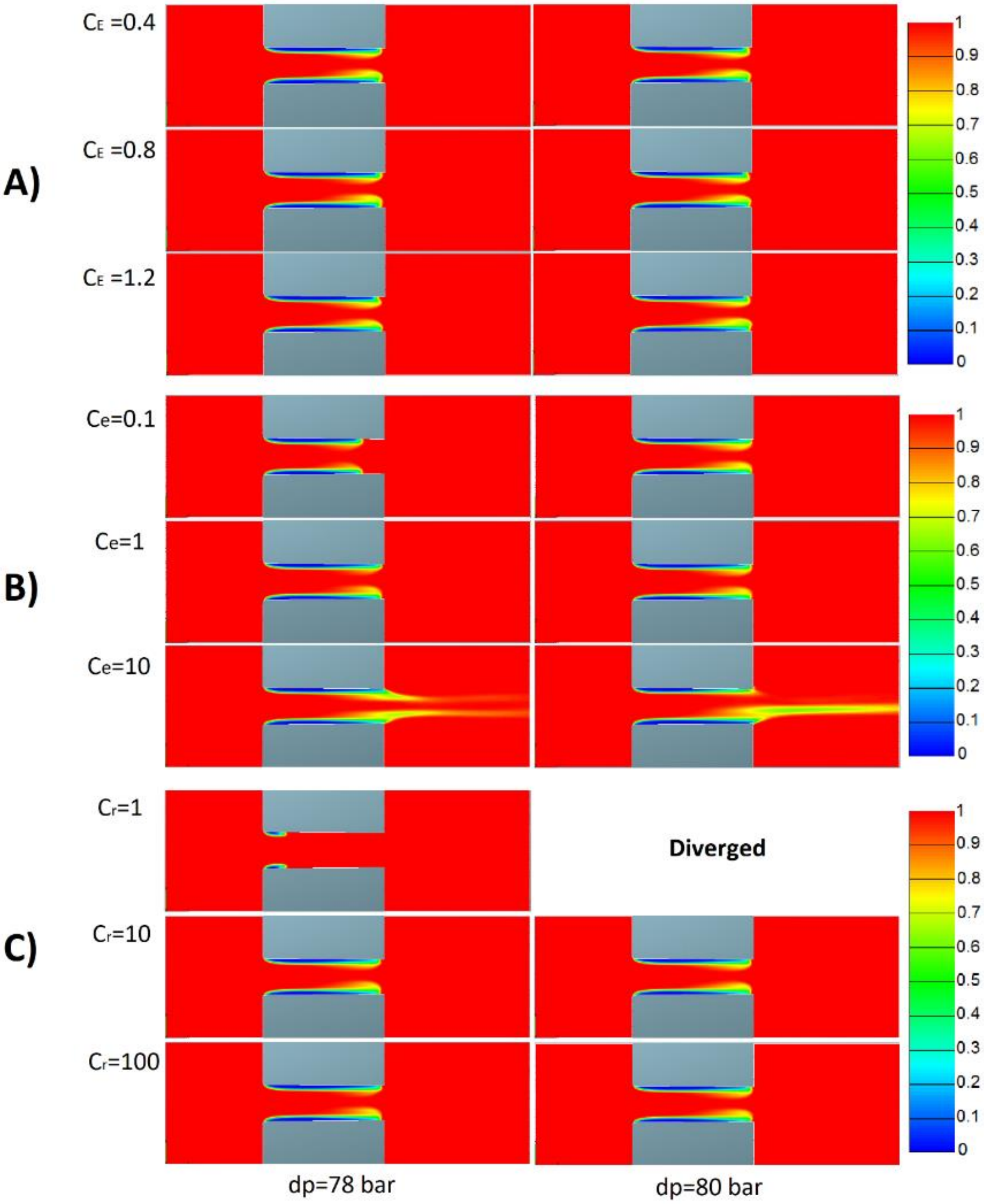

Fig 15 Volume fraction of liquid phase using coefficient sets of Table 4 at the pressure drops of 78 and 80 bar

Finally, Figs. 14c and 15c report on the cavitation region variations obtained with the cavitation reduction factor (C_r) parameter. Inconsistent trends are reported when varying C_r in terms of cavitation growth regions (e.g., increasing growth regions with C_r). The cavitation reduction number should be selected between 10 and 100 to better represent the measured data, especially at critical cavitation threshhold. The cavitation region is significantly underpredicted using a cavitation reduction factor of one. In addition, the effect of increasing the cavitation reduction factor beyond 10 is minimal on the cavitation region, cavitation number, and mass flow rate.

6. Conclusions and Recommendations

Cavitation and erosion models within the AVL-Fire computational fluid dynamics framework have been assessed in detail using a range of models and compared with measured data from a laboratory-scale benchmark nozzle. The assessment included investigating the effect of pressure drop across the nozzle on the cavitation and erosion propensity, quantification of erosion damage, and sensitivity study of the erosion governing parameters

The multiple AVL-Fire models available were compared to existing ARL internal models across nozzle conditions in the range $20 < dP < 85$ bar using *n*-dodecane fuel. The effect of the cell-size distribution on the cavitating flow behavior was studied and grid-converged results were obtained in each case. The AVL-Fire models were able to predict the experimental mass flow rate in the linear region and the choked flow region with slight overpredictions of the time to cavitation onset. Although the experimental uncertainty in the benchmark nozzle was not reported, the models were able to predict the behavior of onset and the fluid-energy exchange mechanism of cloud collapse at the nozzle surface. The predictions were more accurate in terms of volume fraction for the higher injection pressure of $dP = 80$ bar. Velocity profiles at two stations near the nozzle inlet were also accurately predicted and captured the peak intensity region and the shear layer velocity distributions. The erosion damage was predicted using the AVL-Fire models through the MDPR parameter that utilizes the critical distance of bubble collapse as a governing metric. The results showed that the vulnerability zones are strongly dependent on the operating conditions considered and occur in regions extending from the center inlet to the nozzle exit location and correlate with regions of pronounced cavitation intensity. Thus, the maximum damage is likely to occur in the closure area of the vapor region, where the bubbles collapse and when the cavitation region is small. This is corroborated by the significant reduction in MDPR penetration rates for larger cavitation regions.

The findings from this report are summarized as follows:

1) AVL-Fire has a unique modeling capability in terms of predicting multi-dimensional erosion damage than what is domestically and currently available as part of ARL's internal CFD suite.

2) The AVL-Fire cavitation models were able to predict the experimental mass flow rate in the linear region and the choked flow region with slight

overpredictions of the time to cavitation onset. This transition is one of the most important features to predict since it governs the pitting intensity as well as the jet discharge rate. The models were successfully compared against the available experimental data from a benchmark nozzle.

3) AVL-Fire models are able to predict erosion damage through the MDPR metric and the incubation time period considering contributions (inputs) from the impacts per unit area, size of the impact loads, maximum thickness of the hardened layer, and the shape factors. The analysis demonstrated that the damage vulnerability zones are directly related to cavitation intensity and the size of the cavitation region (or vapor closure region). Maximum damage occurs in the closure area of the vapor cloud where bubbles collapse, and increased levels of vorticity and rate of turbulence production are present.

4) The governing parameter-sensitivity study across the operating conditions in this assessment revealed the empiricism that still remains when modeling cavitating flows. Recommendations were made in terms of the model coefficients that best reproduce the experimental data with the available nozzle configuration studied at ARL. Further strategies to mitigate damage can be explored relating to nozzle geometry, fuel composition, and material properties.

Although the implemented models demonstrate the onset of cavitation and cloud collapse events that lead to pitting and material erosion, further basic research needs to be conducted to explain the physical mechanisms governing cavitation. There is a clear need for benchmark experimental cavitation data in canonical configurations with tight control of the boundary conditions, fuel properties, and measurements with reported uncertainties to drive basic modeling efforts. The use of high-fidelity analysis tools with minimal assumptions should also be explored further to reveal microscale mechanisms that are outside of experimental range, such as the bubble collapse processes. The findings reported in this assessment serve as an initial step warranting further basic research to benefit novel designs of innovative Army propulsion technologies.

7. References

1. Shi Y, Ge HW, Reitz R. Computational optimization of internal combustion engines. London (England): Springer; 2011.

2. Chaves H, Knapp M, Kubitzek A, Obermeier F, Schneider T. Experimental study of cavitation in the nozzle hole of diesel injectors using transparent nozzles. Bowie (MD): SAE International; 1995. Report No. 950290. p. 199–211. doi: https://doi.org/10.4271/950290.

3. Soteriou C, Andrews R, Smith M. Direct injection diesel sprays and the effect of cavitation and hydraulic flip on atomization. Bowie (MD): SAE International; 1995. Report No. 950080. p. 27–52. doi: https://doi.org/10.4271/950080.

4. Reitz RD, Bracco FV. Mechanism of atomization of a liquid jet. Physics of Fluids. 1982;25(10):1730–1742.

5. Tamaki N, Nishida K, Hiroyasu H, Shimizu M. Effects of the internal flow in a nozzle hole on the breakup processes of a liquid jet. Proceedings of ICLASS-97; 1997; Seoul, South Korea. p. 417–424.

6. Hiroyasu H, Arai M, Shimizu M. Breakup length of a liquid jet and internal flow in a nozzle. Proceedings of ICLASS-91; 1991; Gaithersburg, MD.

7. Badock C, Wirth R, Tropea C. The influence of hydro grinding on cavitation inside a diesel injection nozzle and primary break-up under unsteady pressure conditions. Proceedings of the 15th Annual Conference on Liquid Atomization & Spray Systems (ILASS-Europe); 1999 July 15–17; Toulouse, France.

8. Shinohara Y, Takeuchi K, Herrmann OE, Laumen HJ. 3000 bar common rail system. MTZ worldwide eMagazine. 2011;72:4-9.

9. Asi O. Failure of a diesel engine injector nozzle by cavitation damage. Eng Fail Analysis. 2006;13(7):1126–1133.

10. Benjami TB, Ellis AT. The collapse of cavitation bubbles and the pressures thereby produced against solid boundaries. Phil Trans Royal Soc London A, Math Phys Sci. 1966;260(1110):221–240.

11. Winklhofer E, Kull E, Kelz E, Morozov A. Comprehensive hydraulic and flow field documentation in model throttle experiments under cavitation conditions. Proceedings of the 17th Annual Conference on Liquid Atomization and Spray Systems (ILASS-Europe); 2001 Sep 2–6; Zurich, Switzerland.

12. Morozov A, Iben U. Experimental analysis and simulation of cavitating throttle flow. Proceedings of the 6th International Conference on Heat Transfer, Fluid Mechanics and Thermodynamics (HEFAT); 2008 June 30–July 2; Pretoria, South Africa.

13. Dabri S, Sirignano W, Jospeh DD. Cavitation in an orifice flow. Physics of Fluids. 2007;19(7).

14. Som S, Aggarwal SK, El-Hannouny EM, Longman DE. Investigation of nozzle flow and cavitation characteristics in a diesel injector. J Eng Gas Turb Power. 2010;132(4).

15. Zhao H, Quan S, Dai M, Pomraning E, Senecal PK, Xue Q, Battistoni M, Som S. Validation of a three-dimensional internal nozzle flow model including automatic mesh generation and cavitation effects. J Eng Gas Turb Power. 2014;136(9).

16. Devassy BM, Edelbauer W, Greif D. Study of cavitation and 3D needle movement due to erosion in fuel injection nozzles using coupled simulation tools. Proceedings of the 18th Annual Conference on Liquid Atomization and Spray Systems (ILASS-Asia); 2016 Nov 6–9; Chennai, India.

17. Bicer B, Sou A. Application of the improved cavitation model to turbulent cavitating flow in fuel injector nozzle. App Math Model. 2016;40(7–8).

18. Schnerr G, Sauer J. Physical and numerical modeling of unsteady cavitation dynamics. Proceedings of the 4th International Conference on Multiphase Flow; 2001 May 27–June 1; New Orleans, LA.

19. Singhal AK, Athavale MM, Li H, Jiang Y. Mathematical basis and validation of the full cavitation model. J Fluids Eng. 2002;124(3).

20. Alajbegvic A, Meister G, Greif D, Basara B. Three phase cavitating flows in high pressure swirl injectors. Exp Ther Fluid Sci (ETF Science). 2002;26(6-7):677–681.

21. Greif D, Monteverde B, Alajbegovic A. Simulation of cavitating flow in high pressure gasoline injectors. Proceedings of the 9th International Conference on Liquid Atomization and Spray Systems (ICLASS); July 13–17; Sorrento, Italy.

22. Drew AD, Passman SL. Theory of multicomponent fluids. New York (NY): Springer; 1999.

23. Lahey RT Jr, Drew DA. An analysis of two-phase flow and heat transfer using a multidimensional, multi-field, two-fluid computational fluid dynamics (CFD) model. Proceedings of the Japan/US Seminar on Two-Phase Flow Dynamics; 2000; Santa Barbara, CA.

24. Kunz RF, Siebert BW, Cope WK, Foster NF, Antal SP, Ettore SM. A coupled phasic exchange algorithm for multi-dimensional four-field analysis of heated flows with mass transfer. Computers and Fluids. 1998;27(7):741–768.

25. Carrica PM, Bonetto F, Drew DA, Lahey RT Jr. A polydispersed model for bubbly two-phase flow around a surface ship. Int J Multiphase Flow. 1999;25(2):257–305.

26. Franklin RE, McMillan J, Rozewicz J. Proc. The stability and concentration of gas micro-bubbles in liquids. ASME International Symposium on Cavitation Inception; 1984; New Orleans, LA. p. 1–8.

27. Fujimoto H, Nishikori T, Hojyo Y, Tsumakoto T, Senda J. Modeling of atomization and vaporization process in flash boiling spray. Proceedings of the 6th International Conference on Liquid Atomization and Spray Systems (ICLASS 94); 1994 July 18–22, Rouen, France.

28. Leighton TG. Derivation of the Rayleigh–Plesset equation in terms of volume. Southampton (UK): Institute of Sound and Vibration Research (ISVR), University of Southampton; 2007. Report No.: 308.

29. Hinze JO. Turbulence. New York (NY): McGraw-Hill; 1975. p. 309.

30. AVL FIRE. Eulerian multiphase user manual. Graz (Austria): AVL; 2017.

31. Berchiche N, Franc JP, Michel JM. A cavitation erosion model for ductile materials. J Fluids Eng. 2002;124:601–606.

32. Franc JP, Riondet M. Incubation time and cavitation erosion rate of work-hardening materials. Proceedings of the 6th International Symposium on Cavitation (CAV2006); 2006 Sep; Wageningen, The Netherlands.

33. Shields B, Neroorkar K, Schmidt DP. Cavitation as rapid flash boiling. Proceedings of the ILASS–Americas 23rd Annual Conference on Liquid Atomization and Spray Systems; 2011; Ventura, CA.

List of Symbols, Abbreviations, and Acronyms

1-D	1-dimensional
3-D	3-dimensional
ARL	US Army Research Laboratory
CC	critical cavitation
CFD	computational fluid dynamics
LES	Large Eddy Simulation
LS	level-set
MDPR	mean depth of penetration rate
MR	Modified Rayleigh
RANS	Reynolds Averaged Navier Stokes
VCO	valve covered orifice
VOF	volume of fluid

1 (PDF)	DEFENSE TECHNICAL INFORMATION CTR DTIC OCA
2 (PDF)	DIRECTOR IMAL HRA RECORDS MGMT RDRL DCL TECH LIB
1 (PDF)	GOVT PRINTG OFC A MALHOTRA
1 (PDF)	US ARMY FOREIGN COMPARATIVE TESTING PROGRAM US ARMY GLOBAL TECHNOLOGY OFFICE (GTO), RDECOM HQ R IMPERIALE
1 (PDF)	US ARMY AVIATION AND MISSILE RESEARCH DEVELOPMENT AND ENGINEERING CENTER AVIATION DEVELOPMENT DIRECTORATE K KERNER
6 (PDF)	DIR ARL RDRL DPT A MARTIN RDRL VTP L BRAVO M MURUGAN A GHOSHAL C KWEON RDRL VTV B GLAZ